Journal of Zhejiang University-SCIENCE A (Applied Physics & Engineering) 2024 25(7):541-556
www.jzus.zju.edu.cn; www.springer.com/journal/11582
E-mail: jzus_a@zju.edu.cn

Research Article

https://doi.org/10.1631/jzus.A2300613

Large eddy simulation study of 3D wind field in a complex mountainous area under different boundary conditions

Yan LI[1], Lei YAN[1,2,3]✉, Xuhui HE[1,2,3]

[1]*School of Civil Engineering, Central South University, Changsha 410075, China*
[2]*National Engineering Research Center for High-speed Railway Construction, Changsha 410075, China*
[3]*Hunan Provincial Key Laboratory for Disaster Prevention and Mitigation of Rail Transit Engineering Structures, Changsha 410075, China*

Abstract: Large eddy simulations generally are used to predict 3D wind field characteristics in complex mountainous areas. Certain simulation boundary conditions, such as the height and length of the computational domain or the characteristics of inflow turbulence, can significantly impact the quality of predictions. In this study, we examined these boundary conditions within the context of the mountainous terrain around a long-span cable-stayed bridge using a wind tunnel experiment. Various sizes of computational domains and turbulent incoming wind velocities were used in large eddy simulations. The results show that when the height of the computational domain is five times greater than the height of the terrain model, there is minimal influence from the top wall on the wind field characteristics in this complex mountainous area. Expanding the length of the wake region of the computational domain has negligible effects on the wind fields. Turbulence in the inlet boundary reduces the length of the wake region on a leeward hill with a low slope, but has less impact on the mean wind velocity of steep hills.

Key words: Large eddy simulation (LES); Spectral representation method; Recycling method; High mountainous canyon; Wind characteristics; Atmospheric boundary layer; Computational domain

1 Introduction

Wind flow patterns in mountainous areas are complex due to their 3D nature (Han et al., 2018; Ren et al., 2018; Jiang et al., 2021; Pirooz et al., 2021; Zhang et al., 2022). Wind fields in mountainous areas are characterized by high turbulence, large attack angles, and non-uniformity (Flay et al., 2019; Jing et al., 2019; Hu et al., 2021; Zhou et al., 2022a). The wind velocity distributions in mountainous areas differ significantly from those in flat areas due to obstruction and deflection effects. Some national and regional standards (AIJ, 2004; CEN, 2005; MOT, 2018; NRCC, 2020; AS/NZS, 2021; ASCE, 2022) recommend the use of a topography factor for simplified hills, but these parameters may not be suitable for complex terrains.

With the rapid development of computing technology, computational fluid dynamics (CFD) has gradually become a popular study method. Compared to field measurements and wind tunnel tests, studying wind fields in complex terrain using CFD is more cost-effective and time-saving, and can obtain wind field characteristics at all locations throughout the entire computational domain. For example, Tang et al. (2020) used the Reynolds-averaged Navier-Stokes model (RANS) to obtain the non-uniform distributions of wind velocities and angles of attack (the angle between the mainstream direction of the wind and the horizontal plane) over hilly terrains. However, large eddy simulations (LESs) perform better in predicting complex terrain wind fields due to their greater ability to predict topographic-induced airflow separation and reattachment (Liu et al., 2016; Ma and Liu, 2017; Yang et al., 2020, 2021; Xing et al., 2021). Chaudhari et al. (2016) predicted the wind characteristics of the complex Bolund hill site using LES. The simulation error of this LES model for predicting turbulent kinetic energy was 19% smaller than that of other models. Flay et al. (2019) also found that LES shows excellent

---

✉ Lei YAN, leiyan@csu.edu.cn
Yan LI, https://orcid.org/0000-0001-5363-2851
Lei YAN, https://orcid.org/0000-0003-3688-8673
Xuhui HE, https://orcid.org/0000-0003-2746-182X

Received Dec. 5, 2023; Revision accepted Feb. 23, 2024; Crosschecked June 17, 2024; Online first July 17, 2024

results in predicting flow fields over natural complex terrain such as Belmont hill. Therefore, LES was used in this study to obtain the wind field of a complex terrain.

The boundary conditions of the calculation domain have a significant impact on the wind field in CFD studies, making it crucial to set appropriate boundaries for accurate simulation. The boundary conditions at the inlet, top, and outlet affect the calculation results of the wind field. The inlet boundary should be set as close to its real situation as possible. In the case of a mountainous terrain model, using a fluctuating wind inlet boundary is more realistic than a uniform one. The top boundary's influence on the calculations is seen mainly in the venturi effect. A shorter top boundary tends to have a more severe venturi effect as air flows through the model, resulting in unintended acceleration of wind velocity. The farther the outlet boundary is from the model, the larger the wake vortex development and dissipation space. Conversely, having an outlet boundary too close to the model can cause serious reflow on the boundary, leading to deviation from the real value and calculation error. The recommended calculation domain size of the topographic wind field calculation in regional standards is relatively large, and 20*L* (where *L* represents the length of the terrain model) is the recommended distance from the outlet to the terrain model (MOT, 2018). However, recent studies on wind fields in complex terrains (Liu et al., 2016; Hu et al., 2018; Tang et al., 2019) have often failed to meet this requirement. Zhang et al. (2018) set the bottom boundary of the computational domain as the surface with the terrain shape, so the terrain model directly extended to the outlet boundary. This method has an extensive terrain range and avoids the "artificial cliff" caused by truncation on the terrain, but there are reverse flows on the outlet, which affect the accuracy of the calculation. Ishihara et al. (2020) highlighted that grid solutions strongly impact the accuracy of LES modeling when simulating turbulent flow fields in urban areas.

A computational domain inlet boundary for wind fields of mountainous areas with added turbulence is reasonable, as the turbulence intensity in these topographies is relatively large. Spectral representation and precursor simulation are general methods for adding turbulence in the inlet boundary in LES. The spectral representation method (SRM) generates a fluctuating wind velocity time history using an inverse Fourier transform. Zhou et al. (2022b) generated a longitudinal fluctuating wind velocity based on the measured experimental spectrum (Ishihara et al., 1999) for six turbulence models. Both of the time histories they generated satisfied the target power spectrum and mean wind velocities. As for the traditional precursor simulation method, a pre-computation domain with spires and floor roughness elements is set and executed before the core calculation (Uchida and Ohya, 2003). The downstream wind velocities in a 2D plane are recorded and saved as time series to be used as the inlet boundary conditions in subsequent simulations. Lund et al. (1998) proposed the recycling method (RM) to reduce the amount of precursor simulation calculations. The wind velocities on a surface downstream of the floor roughness elements are recorded, processed, and then used as the inlet boundary condition of the pre-computation domain. Reducing the number of floor roughness elements reduces the amount of RM calculations. Cao et al. (2012) used the immersed boundary method when performing the RM precursor simulation, which further improved computational efficiency. Turbulence in the inflow can affect the location and extent of the airflow separation at the top of the mountain, impacting wind field characteristics. Wang et al. (2014) simulated a wind field for simplified hills with two types of inlet conditions: uniform inflows and turbulent inflows. With turbulence in the inflow, no airflow separation occurred at the top of a gentle hill, and there was a shorter distance between separation and reattachment points for a steep hill compared to cases without turbulence.

In this study, we calculate the wind field characteristics in a complex mountainous area around a long-span cable-stayed bridge using LES. The terrain model is placed in computational domains of different sizes, referencing the terrain model size, and the wind field characteristics are calculated to explore the influence of the top and outlet boundaries. Uniform and turbulent inflows are set to study the impact of turbulence at the inlet boundary on the wind field.

2 Numerical model

2.1 Site geography and wind tunnel test

Fig. 1 shows the topographic elevation map within 20 km of the mid-span of the long-span cable-stayed bridge. There are four main mountains, and Pylon 1 and Pylon 2 are located at the foothills of Mountains D and C, respectively. The canyon between Mountains A and B is relatively wide, while the canyon between Mountains C and D is narrow.

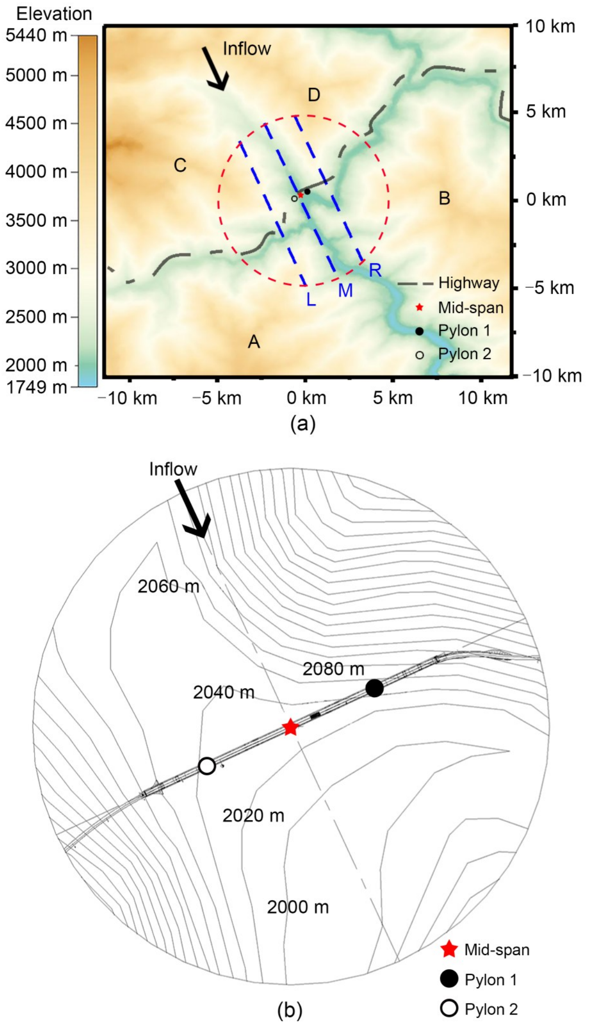

(a)

(b)

Fig. 1 Topographic map of a complex mountainous area and monitored points and lines: (a) 20-km square area around the bridge site; (b) contour map of details near bridge site

A wind tunnel test of the wind field characteristics in the mountainous area was conducted at the TJ-3 boundary layer wind tunnel laboratory at Tongji University, China. The geometric model includes the terrain within a diameter of 10 km around the mid-span, shown within the dotted line (Fig. 1a), and a straight slope transition section is set outside the terrain. The scale ratio of the model is 1:2200, and the diameter of the entire model is 5.5 m. Further details about this experiment can be found in (Yan et al., 2016).

2.2 CFD model

A geometric model, the same as the terrain model in the experiment, was established and placed in the computational domain of the numerical simulation. Fig. 2 illustrates the numerical terrain model. The terrain model is 4.75 m from the left and right walls, and 4.25 m from the inlet boundary.

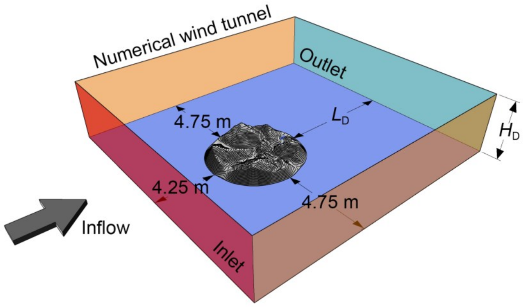

Fig. 2 Sketch map of the computational domain of the numerical wind tunnel. L_D is the distance from the outlet to the terrain model, and H_D is the height of the calculation domain

In the wind tunnel test described in Section 2.1, the height of the test section was 2.0 m, while the height of the terrain model was about 1.0 m, so there was only a small distance between the model and the top wall. In the current numerical wind tunnel test, the model height H_m=1.0 m was used as a reference, and the height of the calculation domain H_D was set as $2H_m$ (the same as in the wind tunnel laboratory), $2.25H_m$, $2.50H_m$, $2.75H_m$, $3H_m$, $4H_m$, $5H_m$, and $6H_m$ for the simulation calculation to explore the influence of the top wall on the wind field characteristics. The computational domain arrangements for the eight calculation domain heights are shown in Table 1.

At the same time, to investigate the impact of the outlet on the wind field characteristics, and using a model diameter of L_m=5.5 m as a reference, the distance from the outlet to the terrain model (L_D) was set at $0.77L_m$ (the same as the wind tunnel laboratory), $2L_m$, $3L_m$, and $5L_m$. The computational domain setups for these four cases are shown in Table 2.

Based on the experimental results, when the approaching flow is 335.2°, perpendicular to the main girder, the mean wind velocity and turbulence intensity are the most unfavorable for the bridge structure.

Table 1 Computational domain arrangements for eight calculation domain heights (model height H_m=1.0 m, model diameter L_m=5.5 m)

Case number	H_D	L_D	Cell number (million)
1	$2H_m$	$0.77L_m$	5.00
2	$2.25H_m$	$0.77L_m$	5.40
3	$2.50H_m$	$0.77L_m$	5.74
4	$2.75H_m$	$0.77L_m$	6.02
5	$3H_m$	$0.77L_m$	6.18
6	$4H_m$	$0.77L_m$	6.74
7	$5H_m$	$0.77L_m$	7.24
8	$6H_m$	$0.77L_m$	7.80

Table 2 Computational domain setups for four distances from the outlet to the terrain model (H_m=1.0 m, L_m=5.5 m)

Case number	H_D	L_D	Cell number (million)
1	$2H_m$	$0.77L_m$	5.00
9	$2H_m$	$2L_m$	5.19
10	$2H_m$	$3L_m$	5.33
11	$2H_m$	$5L_m$	5.56

Therefore, this study focused on investigating an approaching flow direction of 335.2°.

2.3 Computational settings

Prismatic meshes were applied in the above computational domain. Fig. 3 shows the computation mesh near the terrain model. A hexahedral mesh was used in the core areas above the terrain model, as the surface meshes of the model were all quadrilateral. The minimum horizontal mesh size was 0.01 m, and the maximum was 0.03 m. A hybrid mesh of triangular prisms and hexahedrons was used outside the terrain model. The horizontal mesh size near the model was 0.03 m, and as the mesh extended towards the surrounding boundaries, it gradually increased to 0.23 m. By increasing and decreasing the mesh size by 1.1 times, respectively, coarser and finer meshes were obtained. The calculated results of the three meshes were compared with the previous wind tunnel test data, and the results indicated that the normal mesh size was sufficient. From the terrain model surface to the top boundary, the mesh height gradually increased from 0.00045 to 0.04000 m, with a stretching ratio of 1.12. The y^+ value of most areas on the surface of the terrain model did not exceed 3, except for the ridge and peak, where the y^+ value reaches around 10 due to the distortion of the mesh. The total mesh number of the calculation domain with the same size as the wind tunnel laboratory was 5.00 million, and those of other calculation domains are summarized in Table 1.

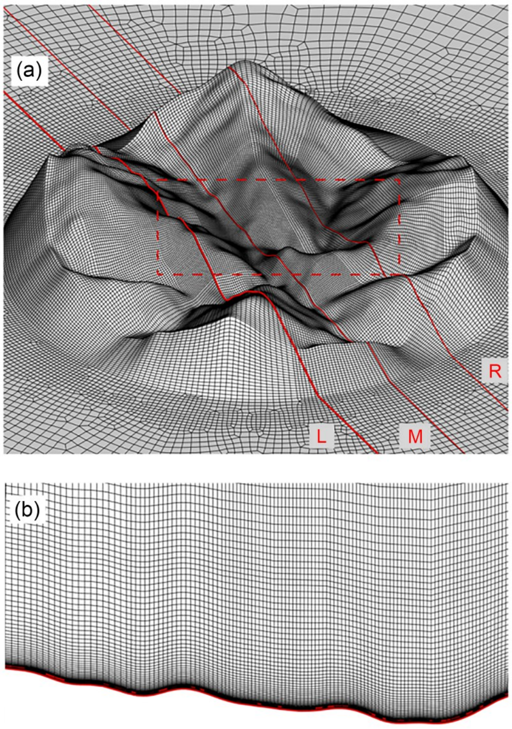

Fig. 3 Computation mesh near the terrain model: (a) mesh of the terrain surface; (b) mesh on a vertical plane through the center of the model (surface M)

The algorithmic details of the numerical simulation are shown in Table 3. The turbulence model used was LES, and the standard Smagorinsky-Lilly model (the Smagorinsky constant C_s=0.1) was used to calculate the subgrid-scale stresses. The spatial discretization and temporal discretization were set as central differencing and bounded second-order implicit, respectively. The SIMPLE (semi-implicit method for pressure-linked equation) algorithm was used for the pressure-velocity coupling method. A time step of

Table 3 Numerical simulation algorithm and parameter setting

Item	Description
Turbulence model	LES
Subgrid-scale model	Smagorinsky-Lilly model
Spatial discretization	Central differencing scheme
Temporal discretization	Bounded second-order implicit time integration
Pressure-velocity coupling method	SIMPLE
Time step	0.001 s
Step of the recorded data	From the 4000th step to the 10000th step

0.001 s was selected for this numerical simulation after considering factors such as the Courant number, computational resources, and the independence validation. The wind velocity data were recorded at each step starting from the 4000th step, when the initial values of the computation domain had minimal impact. A total of 6000 steps were recorded.

2.4 Boundary conditions

The numerical simulation set the inlet boundary condition as the velocity inlet and the outlet boundary condition as the pressure outlet. The two side boundaries were set as symmetrical walls, while the top surface, ground, and terrain model surfaces were set as non-slip walls. To explore the influence of the inflow turbulence on the wind field characteristics in the complex mountainous area, the inlet boundary of Case 1 (where the computational domain size is equal to that of the laboratory experiment) was set as the uniform wind velocity inflow of 12.5 m/s, with time-varying non-uniform wind velocity generated by SRM and RM.

The SRM was implemented by MATLAB code (Cheynet, 2020), and the target mean wind velocity profile was a power law profile:

$$U(z)=U_{\mathrm{G}}\left(\frac{z}{H_{\mathrm{G}}}\right)^{\alpha_0}, \tag{1}$$

where $U(z)$ is the target mean wind velocity at a height of z (m) from the ground. The gradient mean wind velocity U_{G} is equal to 12.5 m/s; the gradient wind height H_{G} was taken as 0.75 m; the surface roughness coefficient α_0 was taken as 0.16. The recommended turbulence intensity for the type B terrain category according to the specification (MOT, 2018) was used as the target value. The target fluctuating wind velocity spectrum was the von Kármán spectrum, and the correlation coefficients were set as $C_{uy}=C_{vy}=C_{wy}=7$ and $C_{uz}=C_{vz}=C_{wz}=10$.

Fig. 4 displays the RM's computational domain size and arrangement of floor roughness elements. The computational domain had a height of 2.0 m, a length of 5.4 m, and a width of 1.5 m. Fifteen rows of 9-cm cubic blocks were arranged uniformly in a staggered manner on the ground. The distance between the floor roughness elements was 0.41 m, and the corresponding density was 6%. In each time step during the simulation calculation, the wind velocities on the recycling boundary at 0.16 m behind the last row of floor roughness elements were recorded and calculated as follows:

$$\begin{cases} u_{\mathrm{in}}(y,z,t)=U(z)+\phi(\eta)\times\left\{u_{\mathrm{re}}(y,z,t)-\bar{u}_{\mathrm{re}}(y,z)\right\}, \\ v_{\mathrm{in}}(y,z,t)=\phi(\eta)\times\left\{v_{\mathrm{re}}(y,z,t)-\bar{v}_{\mathrm{re}}(y,z)\right\}, \\ w_{\mathrm{in}}(y,z,t)=\phi(\eta)\times\left\{w_{\mathrm{re}}(y,z,t)-\bar{w}_{\mathrm{re}}(y,z)\right\}, \end{cases} \tag{2}$$

where y is the spanwise coordinate value; t is the current flow time; u_{in}, v_{in}, and w_{in} are the instantaneous wind velocities of the longitudinal, transverse, and vertical components at the inlet boundary, respectively. The calculated u_{in}, v_{in}, and w_{in} were loaded on the inlet boundary as the inflow of the computational domain shown to implement RM (Fig. 4). u_{re}, v_{re}, and w_{re} represent the fluctuating wind velocities of the longitudinal, transverse, and vertical components on the recycling boundary, respectively; $\bar{u}_{\mathrm{re}}$, $\bar{v}_{\mathrm{re}}$, and $\bar{w}_{\mathrm{re}}$ are the corresponding mean wind velocity components; $\phi(\eta)$ is the weighting function, defined as:

$$\phi(\eta)=\frac{1}{2}\left\{1-\frac{\tanh\left[\dfrac{8.0(\eta-1)}{0.82-0.4\eta}\right]}{\tanh(8.0)}\right\}, \quad \eta=\frac{z}{H_{\mathrm{G}}}, \tag{3}$$

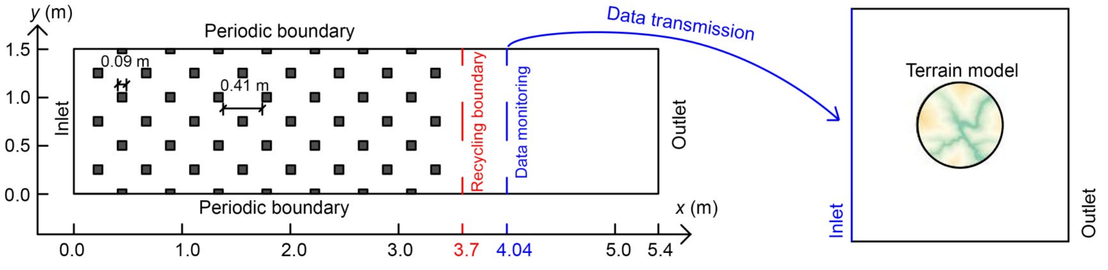

Fig. 4 Configuration of numerical wind tunnel simulating arrangement of floor roughness elements

where η is the normalized height by H_G. During the calculation, the wind velocity at each time step at 0.5 m behind the last row of floor roughness elements was recorded and then used as the inlet boundary condition when the calculation domain contained an executed terrain model (Fig. 2).

Fig. 5 illustrates the vertical profiles of the mean wind velocity and turbulence intensities of the wind velocity time histories generated by SRM and RM. Here, I_u, I_v, and I_w represent longitudinal, transverse, and vertical turbulence intensities, respectively. The uniform inflow is also depicted in this figure. The mean wind velocity profile obtained through SRM followed a power law with a gradient mean wind velocity of 12.5 m/s, precisely reaching the target value. However, the floor roughness elements significantly impacted the mean wind velocity profile obtained by the RM. The mean wind velocity below 0.3 m was lower than that obtained through SRM, while the mean wind velocity above 0.3 m was slightly higher, and the gradient mean wind velocity was 12.8 m/s. The fluctuating wind velocity time histories generated by SRM had a high turbulence intensity at high altitudes, while those generated by RM had a turbulence intensity approaching zero (Fig. 5b). In the computational domain of RM, the vortices consisted only of the wake of the floor roughness elements on the ground, so the wind field with high turbulence intensity was concentrated below a height of 0.5 m. Therefore, the turbulence intensity of RM below a height of 0.3 m was higher than that of SRM. I_w was set to half of I_u, and I_v was 0.88 times I_u when generating wind velocity using SRM, while I_u, I_v, and I_w of the RM were obtained automatically by floor roughness elements, and there was no fixed proportional relationship.

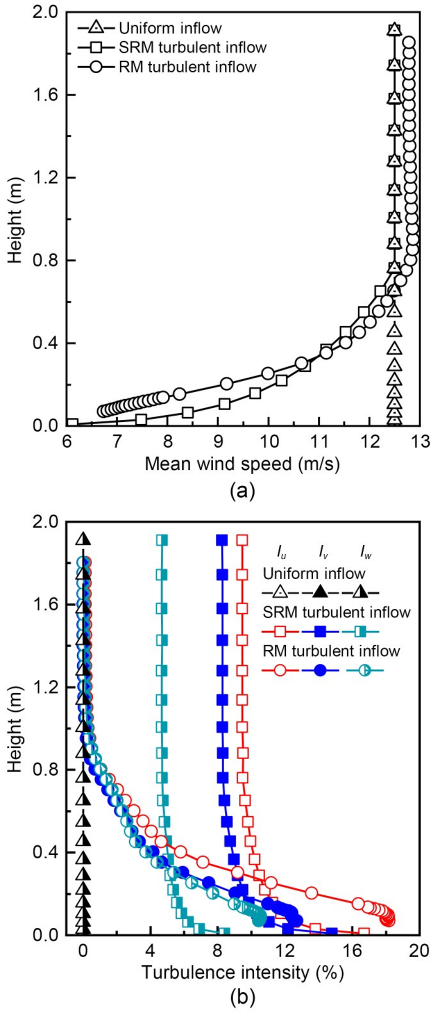

Fig. 5 Wind velocity profiles at the inlet boundary: (a) mean wind velocity profile; (b) turbulence intensity profile

3 Results and discussion

3.1 Verification and wind characteristics of numerical simulation

The mean wind velocity was normalized by the gradient wind velocity of 12.5 m/s in the following simplified analyses. Fig. 6 shows the longitudinal component's normalized mean velocity (U_{nor}) and standard deviation (σ_u) at the two pylons obtained through wind tunnel tests (EXP) and LES. Compared with EXP, the error of LES's normalized mean wind velocity is higher at low velocity than at high velocity. As the velocity increases, the error gradually decreases, with LES's normalized mean wind velocity slightly smaller than the EXP value. The simulated value of the standard deviation of the longitudinal component at most of the monitoring points is higher than the EXP value. However, the relative error between LES and EXP is not higher than 20%, except for a few points where the mean velocity is low. The correlation coefficient of the normalized mean velocity between LES and EXP is 0.99, while the correlation coefficient of the standard deviation of the longitudinal component is relatively low, but higher than 0.95 for both pylons. In summary, the normalized mean velocity and standard deviation of the longitudinal component of the numerical simulation exhibit minor errors compared with the experimental values, and the trend between them is consistent, so the numerical simulation results are credible.

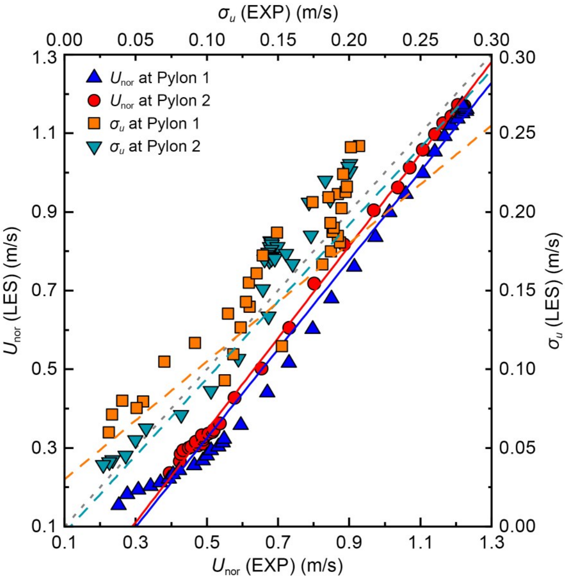

Fig. 6 Scatterplot of simulated and experimental normalized mean velocity and standard deviation of longitudinal component of turbulence. Lines were generated from the linear regression (x and y represent the variables of EXP and LES, respectively. The regression formulas for the normalized mean velocity of Pylon 1 and Pylon 2 are: y=1.13x−0.24, R^2=0.99; y=1.17x−0.24, R^2=0.99. The regression formulas for the standard deviations of Tower 1 and Tower 2 are: y=0.75x+0.03, R^2=0.95; y=0.98x−0.004, R^2=0.98). References to color refer to the online version of this figure

Fig. 7 shows the streamlines through the monitored points and above the terrain model. The topography divides the inlet airflow into two parts, one of which turns into the canyon and flows towards the monitored points in a relatively stable condition. When this part of the airflow passes through the monitored points, it flows in different directions due to the blocking effect of the mountains. Another part of the airflow passes over the upper mountain, the wind velocity decreases, and a large number of eddies are generated on the leeward side. The airflow at Pylon 1 is attributable mainly to the stable wind velocity flowing along the canyon, while the airflow on Pylon 2 is seriously affected by the varying wind velocity on the leeward side, resulting in the complexity of the wind field. The airflow far from the monitored points moves mainly in the upward direction when flowing through the model with increased wind velocity, and then gradually slows down as it flows with the terrain.

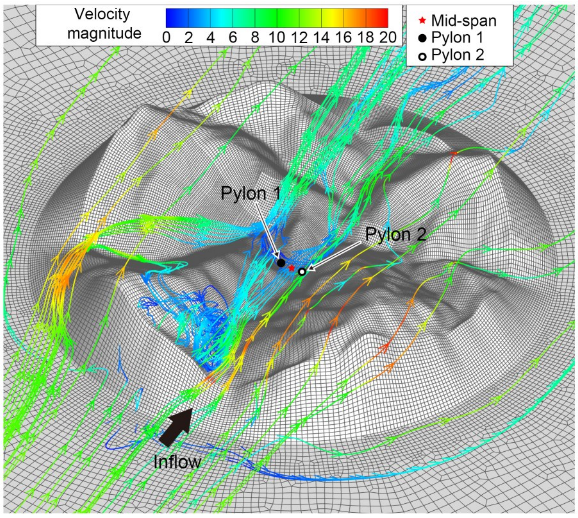

Fig. 7 Streamlines of mean wind velocity above the terrain model and through monitored points. References to color refer to the online version of this figure

The Q-criterion can be calculated by the following formula:

$$Q=\frac{1}{2}\left(|\Omega|^2+|S|^2\right), \tag{4}$$

where Ω and S are the anti-symmetric and symmetric components of the velocity gradient tensor. The positive iso-surface of the Q-criterion indicates the position of the same vorticity in the flow field. Fig. 8 shows a snapshot of the iso-surfaces of the Q-criterion with values equal to 1000. The iso-surfaces are colored based on the magnitude of the velocity. Due to obstruction by the model, vortices form in a semicircular pattern near the ground on the model's windward side. As highlighted by the black rectangle in

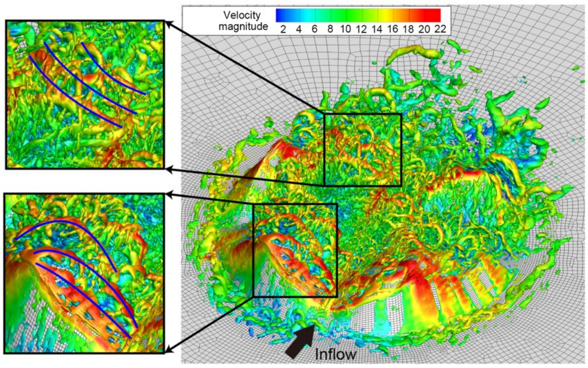

Fig. 8 Instantaneous flow field visualized by iso-surfaces of Q-criterion with values equal to 1000. References to color refer to the online version of this figure

the figure, multiple band-like vortices shedding from the leading edge of the terrain model indicate airflow separation occurring there. In the canyon where the monitored points are located, vortices are finely divided and have no apparent regularity in shape. This phenomenon is due to the local topography. The spiral vortices shed from the ridges at the rear of the model, and then dissipate and disappear 1.5 m downstream of the terrain model. The entire terrain model is covered with abundant vortices, especially close to the ground, where the vortices are fine and 3D.

3.2 Influence of computational field height on wind characteristics

Fig. 9 shows the contour of the pressure distribution at the top boundary of the computational domain. The solid black line represents the profile of the terrain, while the black dotted line represents the profile of the overall model. As the airflow passes through the model, the top boundary is stressed by the airflow due to the obstruction, creating a positive pressure area upstream of the model and a negative pressure area at the model location. In the case where H_D is $2H_m$, the pressure on the top boundary is high and the maximum negative pressure is 30 Pa. The pressure distribution is significantly influenced by the mountain altitude; as the altitude increases, the negative pressure increases. The positive and negative pressures on the top boundary both decrease with the increase of the computational domain. Compared with the computational domain at the height of $2H_m$, the magnitude of the pressure at the top boundary of the $3H_m$ height case is reduced by 50%. The greater the absolute value of the top boundary pressure, the more pronounced the narrow tube effect on the model, and the greater the wind velocity at the terrain model. Simultaneously, the high pressure restricts the development of the vortex structure over the model and reduces the turbulence intensity.

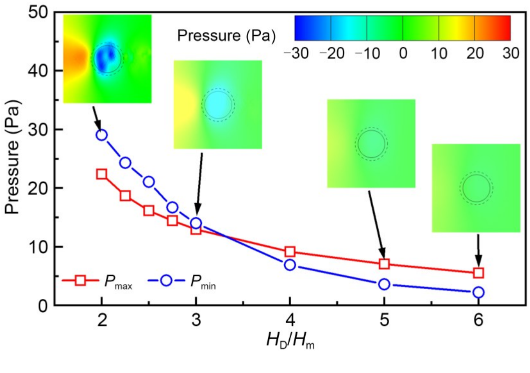

Fig. 9 Magnitude and distribution of pressure at the top boundary on computational domains with different heights. References to color refer to the online version of this figure

Meanwhile, the distribution of the negative pressure does not change with the mountain altitude, but is concentrated in the model's center. The pressure reduction becomes slower when the computational domain is higher than $4H_m$. In the case where H_D is equal to $6H_m$, there are no longer prominent positive and negative pressure zones on the top boundary. The maximum pressure, only 5.5 Pa, is near the inlet boundary, and the pressure in the other areas is about zero.

Fig. 10 shows the variation of the normalized wind velocities with H_D at different heights at the pylons and the mid-span. The trend of the wind velocities at the three locations is similar, and as the computational domain becomes higher, the wind velocities at all locations gradually decrease. The normalized mean wind velocity decreases quickly when the H_D increases from 2.0 to 3.0 m. The mean wind velocity at the height of 0.25 m decreases most rapidly with the increase of H_D, which indicates that the mean wind velocity is more affected by H_D in the lower area than in the upper area.

Fig. 11 displays the normalized mean velocity profiles at the two pylons. The change in H_D significantly impacts the normalized mean velocities. When H_D exceeds $2.50H_m$, the near-wall mean wind velocity profiles exhibit an S-shape, which becomes more pronounced with increasing H_D. When H_D is greater than $3H_m$, the near-wall velocity profiles maintain the S-shape and no longer change with the increase of H_D. The section size of the computational domain increases as the H_D increases, so the narrow tube effect caused by the model decreases, and then the normalized mean velocity in the high altitude also gradually decreases. When H_D increases from $2H_m$ to $3H_m$, the normalized mean velocities at Pylon 1 and Pylon 2 decrease by 0.204 and 0.196, respectively, at the height of 0.4 m. However, when H_D increases from $3H_m$ to $5H_m$, the normalized mean velocities at the two pylons decrease by 0.048 and 0.082, respectively, at the same height. When H_D exceeds $5H_m$, the mean wind velocity hardly changes with the increase of H_D. Therefore, as H_D increases, the influence of the top wall on the normalized mean velocities at the monitored points gradually decreases.

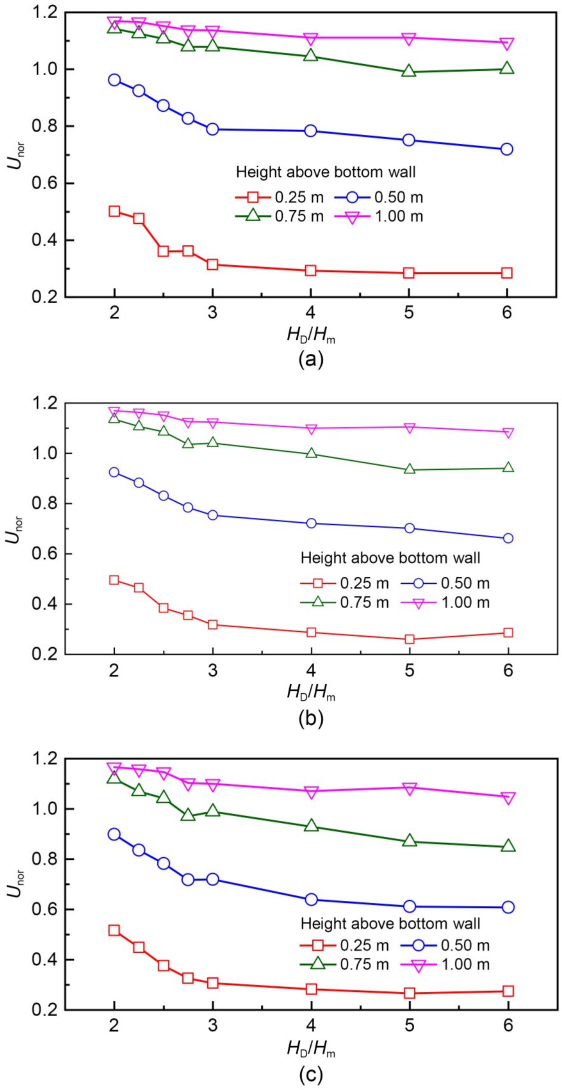

Fig. 10 Variation of normalized mean wind velocities with the height of the computational domain at (a) Pylon 1, (b) mid-span, and (c) Pylon 2

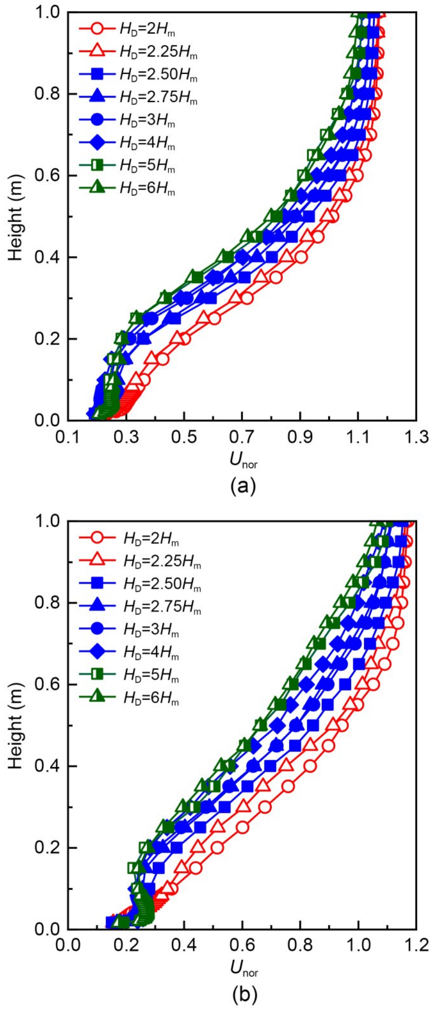

Fig. 11 Profiles of normalized mean wind velocity at (a) Pylon 1 and (b) Pylon 2 simulated through different computational domain heights

Fig. 12 shows the profiles of the standard deviation of the longitudinal component σ_u at the two pylons with different computational domain heights. The variation of σ_u with the changes of H_D is not entirely regular, as the pylon is in the wake vortex of the mountain ahead. When H_D changes, the shape of the profile below 0.15 m changes significantly, while above 0.15 m it does not. As the height increases, σ_u reaches its maximum at a height of 0.4 m and then decreases. When the height is higher than 0.4 m, σ_u increases with H_D, indicating that as H_D increases, the development of turbulent vortices is no longer constrained by the top boundary, so a fluctuating wind velocity gradually develops at high heights. According to the order of H_D, the average relative error of the monitoring points below 1 m was calculated successively between the two cases. When the relative error falls below 0.1, it is considered that σ_u no longer changes significantly with the increase of H_D. At Pylon 1, the relative error of σ_u decreases to 0.093 at $5H_m$. For Pylon 2, the corresponding value is $4H_m$.

3.3 Influence of wake region length on wind characteristics

Fig. 13 illustrates the normalized mean wind velocity profiles at the two pylons with different distances from the outlet to the terrain model (L_D). L_D has minimal impact on the normalized mean velocity. The absolute deviation of the normalized mean velocity caused by the change of L_D at Pylon 1 is less than

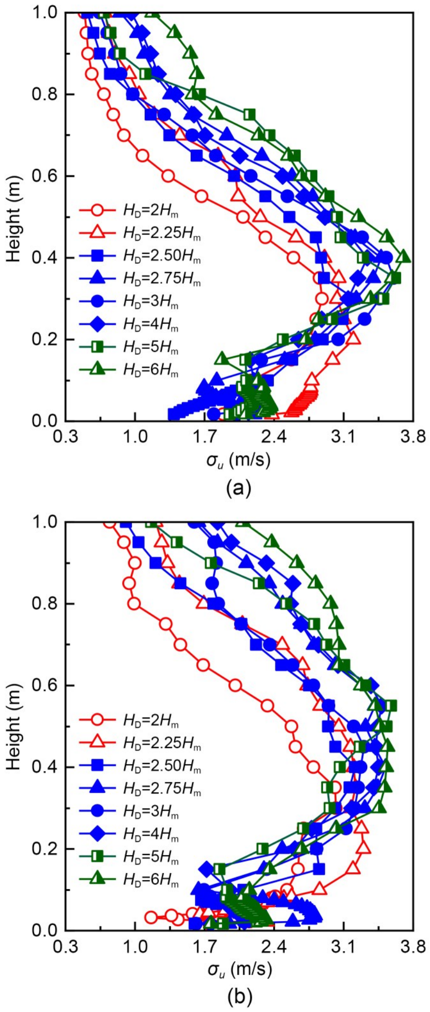

(a)

(b)

Fig. 12 Profiles of standard deviation of the longitudinal component of turbulence at (a) Pylon 1 and (b) Pylon 2 simulated through different computational domain heights

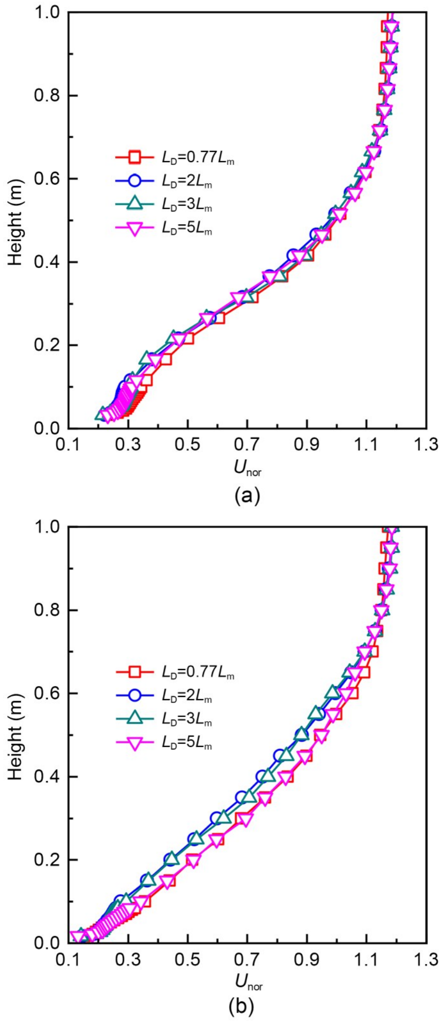

(a)

(b)

Fig. 13 Profiles of normalized mean wind velocity at (a) Pylon 1 and (b) Pylon 2 simulated with different distances from outlet to terrain model

0.05. The absolute deviation at Pylon 2 in the height range of 0.1–0.6 m is larger than that at other locations, and the normalized mean velocity of the L_D equal to $0.77L_m$ and $5L_m$ is about 0.08 larger than that of $2L_m$ and $3L_m$ in the height range of 0.1–0.6 m. Due to the complexity of the wind field at the pylon, there is high fluctuation in wind velocity with an irregular distribution pattern. Simulation calculation error can be considered to be the cause of the previously mentioned deviation.

Fig. 14 shows the profiles of the standard deviation of the longitudinal component σ_u at the two pylons corresponding to the above cases. With the extension of the computational domain, no significant variation is observed at the two pylons below 0.4 m, while σ_u slightly increases above a height of 0.4 m. The increase of σ_u at Pylon 2 is higher than that at Pylon 1, with a maximum increase of 0.38 m/s. This indicates that the outlet boundary limits the development of the fluctuating wind velocity over the model with a small L_D, but the overall impact of the L_D is minimal. Compared to other cases, the σ_u at Pylon 2, where L_D is equal to $2L_m$, is larger at a height of 0.1–0.4 m. One possible reason for this is that the fluctuating wind velocity in this area is high, as it is located on the leeward side of the mountain, and the simulation calculation is prone to overestimating the turbulence intensity.

The study of the distance from the outlet to the terrain model L_D indicates that the outlet boundary does not significantly affect the normalized mean wind velocity at the monitored points, and has minimal impact on the fluctuating wind velocity. Considering that expanding the computational domain will increase computational workload, the L_D of $0.77L_m$ can be considered appropriate for use in engineering applications.

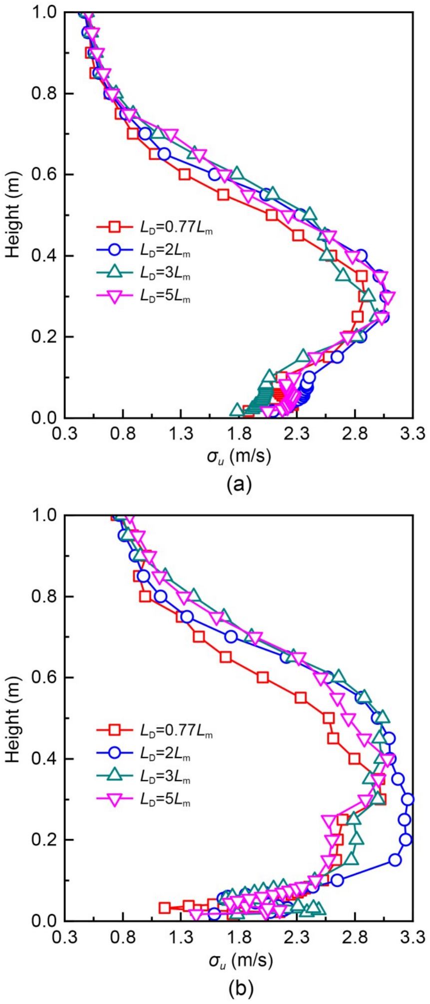

(a)

(b)

Fig. 14 Profiles of standard deviation of the longitudinal component of turbulence at (a) Pylon 1 and (b) Pylon 2 simulated with different distances from outlet to terrain model

3.4 Influence of inlet boundary condition on wind characteristics

To study the wind velocity distribution in the longitudinal direction, the normalized mean wind velocity was calculated at different heights along lines L, M, and R (Fig. 1). Line M passes through the midspan, and the horizontal distance between line L and line M, as well as that between line R and line M, is 0.8 m. Fig. 15 shows the contours of the negative longitudinal velocity component on the planes along lines L, M, and R. The dark green area in the figure represents the outline of the terrain model, while the colored areas with negative velocity indicate recirculation zones. The shapes of the sections cut by lines L, M, and R are notably different. The section cut by line L has a transition line with a slight slope, and the elevation behind it is less undulating (Figs. 15a, 15d, and 15g). This section does not generate significant recirculation zones, with all three inflow conditions behind the transition section. Only small areas of negative velocities are observed in front of the mountain at the downstream location of the model. In Figs. 15b, 15e, and 15h, a steep transition line can be seen upstream of the section cut by line M, and the elevation behind the transition line on this section decreases rapidly and remains low. The turbulent components in the inflow reduce the backflow of this section. As the inflow is uniform, the recirculation area is large and round, with a length of 0.71 m and a height of 0.28 m. Turbulence generated by the RM dramatically reduces the area of the recirculation zone, shortening its

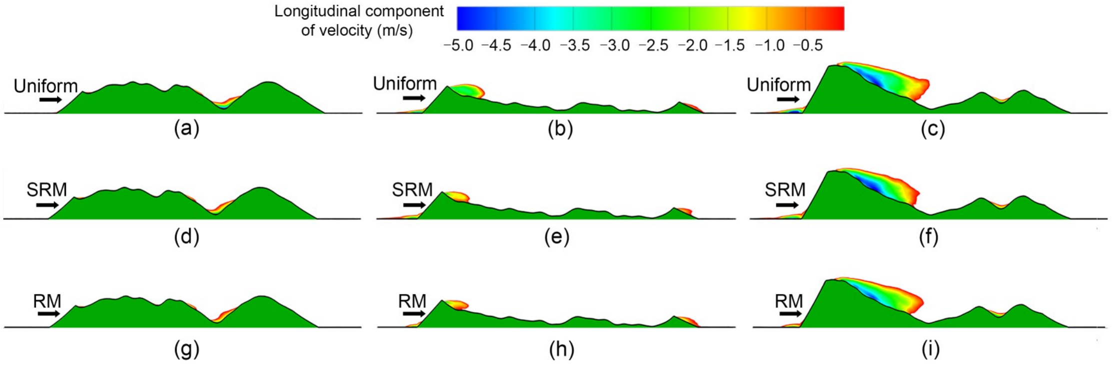

(a) (b) (c)

(d) (e) (f)

(g) (h) (i)

Fig. 15 Contours of regions with a negative longitudinal component of velocity on the planes along lines L (a, d, and g), M (b, e, and h), and R (c, f, and i) with uniform inflow (a, b, and c), SRM inflow (d, e, and f), and RM inflow (g, h, and i). References to color refer to the online version of this figure

length to 0.49 m and its height to 0.18 m. In the SRM case, the length of the recirculation zone in this section is 0.51 m, and the height is 0.19 m. The slope of the transition line and terrain model on the section cut by line R is relatively steep (Figs. 15c, 15f, and 15i). The recirculation zones in this section are large, and the turbulence in the inflow cannot shrink them. Additionally, the recirculation zones of uniform inflow and of turbulent inflow generated by SRM and RM are 1.82, 1.65, and 1.86 m in length, respectively.

Fig. 16 depicts the variation of the normalized mean wind velocity along lines L, M, and R at 0.1 m above ground. The bold solid line represents the topographic line along the lines L, M, and R, the red dotted line is the position 0.1 m above ground level, and the origin point of the abscissa is the center of the terrain model. At this specific height, the magnitude of the velocity of the uniform inflow case (12.5 m/s) is the largest, while the cases of turbulent inflow do not reach the gradient mean wind velocity. The turbulent inflow generated by RM has the lowest normalized mean wind velocity, but the highest turbulence intensity. The normalized mean wind velocity of the three cases decreases rapidly in front of the transition line (−2.5 m on the abscissa in Fig. 16) and increases to be higher than the inflow wind velocity at the transition line. After the transition line, there is no sudden change in the velocity value, and it is greatly affected by the magnitude of the velocity on the inlet boundary. Recirculation zones appear at lines R and M, so the normalized mean wind velocity behind the transition line decreases to about 0.1 within 0.4 m of horizontal distance. On the plane along line M, the turbulence generated by the RM produces the minimal recirculation zone, which causes a low normalized mean wind velocity of 0.1 for the smallest duration, and 0.2 higher than that of the uniform inflow case behind the recirculation area (−1.0 to 0 m on the abscissa). The turbulence in the inflow slightly interferes with the airflow separation on the section cut by line R as the slope of the transition line is steep, so the mean wind velocity distribution is similar across the three cases in the range of −2.0 to 0 m on the abscissa.

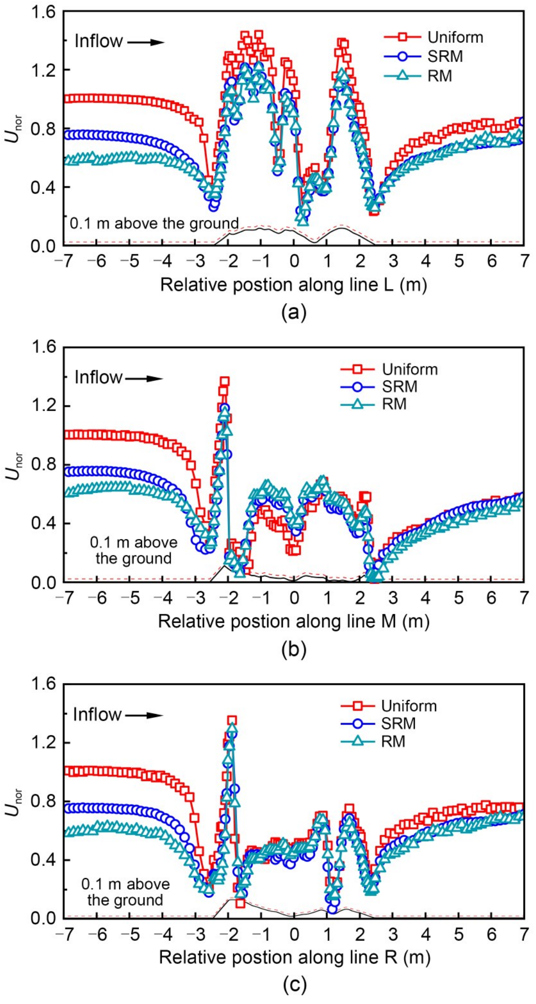

Fig. 16 Normalized mean wind velocity at 0.1 m above ground level (red dotted line) along (a) line L, (b) line M, and (c) line R. References to color refer to the online version of this figure

The wind velocities of the three inflow conditions are similar at a height of 1.0 m above ground. The uniform inflow case and RM case do not have any turbulence at this height, while the inflow generated by SRM has a high turbulence intensity. Fig. 17 shows that the terrain model no longer causes the normalized wind velocities at 1.0 m to vary as dramatically as at 0.1 m height on the planes along lines L and M. The normalized wind velocities increase along the lines at −2.5–−1.0 m on the abscissa, reach the maximum at −1.0 m, and then gradually decrease. The maximum mean wind velocity of the SRM case is lower than those of the other two cases because of the turbulence in the inflow, and the velocity magnitude decays the fastest. The mean wind velocity at the plane along line R still significantly changes with the topography at 1.0 m above ground due to the highest recirculation zone. The normalized mean wind velocity decreases rapidly at −1.0–0 m, and reaches the minimum of 0.7 at the model's center. Airflow separation at the plane along line R has a slight effect on inflow turbulence, and the distribution of the mean

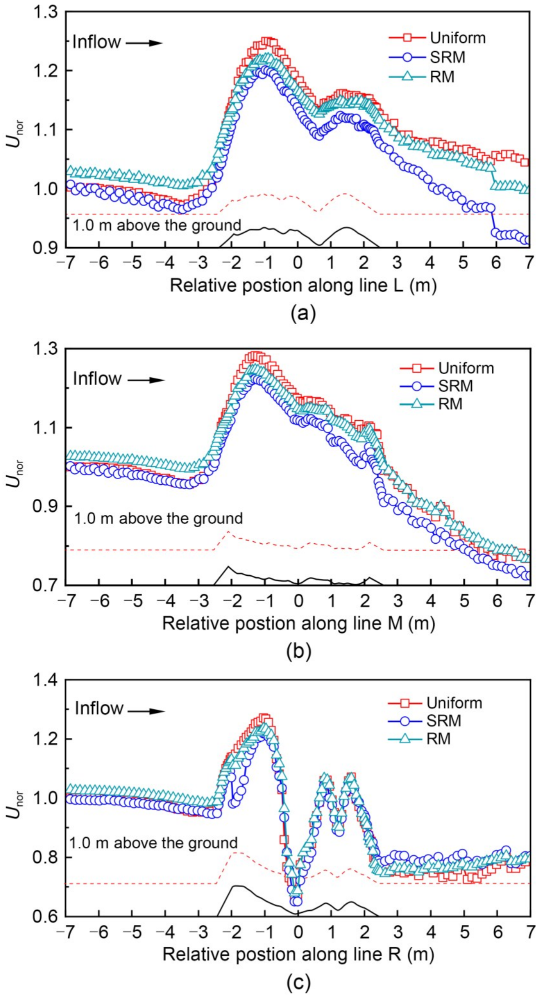

Fig. 17 Normalized mean wind velocity at 1.0 m above ground level (red dotted line) along (a) line L, (b) line M, and (c) line R. References to color refer to the online version of this figure

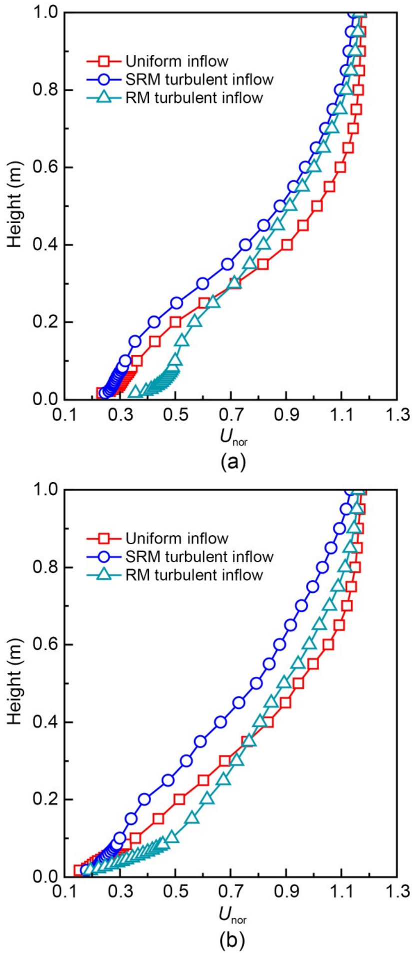

Fig. 18 Profiles of normalized mean wind velocity at (a) Pylon 1 and (b) Pylon 2 simulated with different inlet boundary conditions

wind velocity of the three cases at −1.0–2.0 m almost coincides.

Fig. 18 shows the vertical profiles of the normalized mean wind velocities at the two pylons. Under three different inflow conditions, the shapes of the mean wind velocity profiles at the inlet boundary differ significantly, but those at the pylons are similar. Consequently, the shapes of the mean wind velocity profiles at the monitored points in the canyon are determined mainly by the upstream topography, and the inlet boundary condition has little effect on them. Compared with that of the uniform inflow case, the normalized mean velocity at the pylons in the SRM case is smaller, and the deviations between them are mainly in the height range of 0.2 to 0.8 m. The deviation near the ground and at high height is slight, as the maximums are 0.15 and 0.17 at both pylons. The fluctuating flow generated by the RM has a greater influence than that generated by SRM. The normalized mean velocity in the RM case at Pylon 1 is 0.13 higher than that in the uniform inflow case under 0.1 m height. However, when the height exceeds 0.3 m, the normalized mean velocity of the RM case becomes lower than that of the uniform case, with a maximum absolute deviation of 0.096 at a height of 0.5 m. At Pylon 2, the normalized mean velocity of the RM case has little deviation compared to the uniform flow case below 0.10 m, and the influence of the RM inlet is similar to that of Pylon 1 above 0.10 m.

Fig. 19 shows the profiles of the standard deviation of the longitudinal component σ_u obtained by LES under three different inflow conditions. Compared with the uniform inflow case, the SRM case has

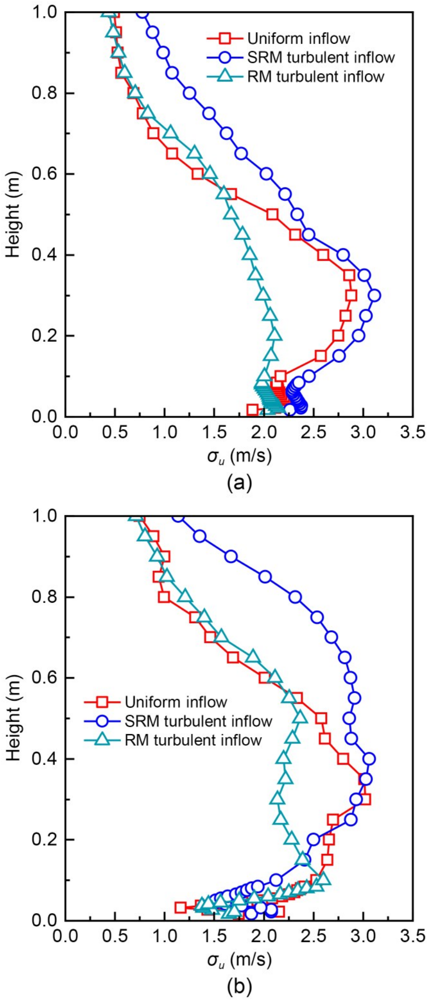

(a)

(b)

Fig. 19 Profiles of standard deviation of the longitudinal component of turbulence at (a) Pylon 1 and (b) Pylon 2 simulated with different inlet boundary conditions

a similar σ_u profile shape at Pylon 1, but a higher magnitude at all heights. When the height is 0.65 m, the σ_u of the SRM case is 1.77 m/s, and the σ_u of the uniform inflow case is 1.08 m/s. The difference between the two cases reached a maximum of 0.69 m/s. At Pylon 2, the inflow generated by SRM increases the σ_u above 0.35 m height, and the increasing magnitude exceeds 1.00 m/s at heights of 0.65–0.85 m. The shape of the σ_u profile at the two pylons obtained in the RM case is quite different from the others. At the inlet boundary of the RM case, the turbulence vortices are concentrated mainly below 0.75 m, but the σ_u values at the pylons are smaller compared to those in the uniform inflow case. When the height is higher than 0.60 m, the deviation between the σ_u of the RM case and the uniform inflow case is minimal. At the lower height of Pylon 1, the σ_u of the uniform inflow case first increases and then decreases with the height, and the maximum value is 2.88 m/s at 0.30 m height. However, the increase of σ_u with the height is very slight in the RM case, and the maximum of the σ_u is only 2.11 m/s at 0.20 m height. In the uniform inflow case, the σ_u increases with the increase of height at Pylon 2 at 0.05–0.30 m. The σ_u of RM case decreases with the increase of height at 0.10–0.25 m, increases slowly at 0.30–0.50 m, and then decreases with the height above 0.50 m. The σ_u of the RM case is 0.88 m/s smaller than that of the uniform inflow case at 0.30 m height.

5 Conclusions

In this study, the effects of the inlet, outlet, and top boundaries on the wind field in a complex mountainous area were investigated by LES, with the following main conclusions:

1. The top boundary greatly influences the wind field in a complex mountainous area when the height of the computational domain (H_D) is lower than triple the height of the terrain model. As the H_D increases, the mean wind velocity decreases while the standard deviation of the longitudinal component of turbulence increases. The change of the wind field characteristics with the change of H_D slows down when H_D is greater than triple the model height. H_D slightly influences the wind field if it is greater than five times the model height.

2. The outlet boundary of the computational domain has minimal impact on the wind field characteristics in a complex mountainous area. A wake region length of 0.77 times the model length was sufficient to satisfy the calculation accuracy in this study. This is because the direct impact of the outlet on the wind field in the complex mountainous area was avoided by the high mountain between them.

3. The inlet turbulence has little effect on the shape of the mean wind velocity profile, but significantly influences the profile of the standard deviation of the longitudinal component of turbulence. When obtaining information about the mean wind velocity, a simple and computationally inexpensive uniform inflow is sufficient. Compared to the uniform inflow, the turbulent inflow generated by the SRM increases the fluctuating wind velocity at a high altitude. On the

other hand, the turbulent inflow generated by the RM significantly reduces the fluctuating wind velocity near ground level. The fluctuating wind velocity produced by the RM is more realistic and is recommended when there are sufficient computing resources.

4. There is a significant impact on the airflow separation of the turbulence in the inlet when the terrain slope is gentle, and the length of the wake area reduces as a consequence of introducing turbulence. However, when the slope is steep, changes in the wind field due to inlet turbulence are limited, as the wind velocity on the leeside of the mountain is affected mainly by the shape of the terrain.

Acknowledgments

This work is supported by the National Natural Science Foundation of China (Nos. 51925808 and 52178516) and the Natural Science Foundation of Hunan Province (Nos. 2020JJ5745 and 2023JJ20073), China.

Author contributions

Yan LI: validation, formal analysis, investigation, data curation, writing of the original draft. Lei YAN: conceptualization, resources, writing–review & editing, supervision, project administration, funding acquisition. Xuhui HE: conceptualization, supervision, funding acquisition.

Conflict of interest

Yan LI, Lei YAN, and Xuhui HE declare that they have no known competing financial interests or personal relationships that could have appeared to influence the work reported in this paper.

References

AIJ (Architectural Institute of Japan), 2004. Recommendations for Loads on Buildings/Commentary, AIJ-2004. AIJ, Tokyo, Japan.

AS/NZS (Australian/New Zealand Standard), 2021. Structural Design Actions. Part 2: Wind Actions, AS/NZS 1170.2: 2021. Australian/New Zealand Standard.

ASCE (American Society of Civil Engineers), 2022. Minimum Design Loads for Buildings and Other Structures, ASCE 7-22. ASCE, Reston, USA.

Cao SY, Wang T, Ge YJ, et al., 2012. Numerical study on turbulent boundary layers over two-dimensional hills—effects of surface roughness and slope. *Journal of Wind Engineering and Industrial Aerodynamics*, 104-106:342-349. https://doi.org/10.1016/j.jweia.2012.02.022

CEN (European Committee for Standardization), 2005. Eurocode 1: Actions on Structures—Part 1-4: General Actions—Wind Actions, BS EN 1991-1-4:2005. British Standard.

Chaudhari A, Hellsten A, Hämäläinen J, 2016. Full-scale experimental validation of large-eddy simulation of wind flows over complex terrain: the Bolund hill. *Advances in Meteorology*, 2016:9232759. https://doi.org/10.1155/2016/9232759

Cheynet E, 2020. Wind Field Simulation (Text-Based Input). Zenodo. https://doi.org/10.5281/ZENODO.3823864

Flay RGJ, King AB, Revell M, et al., 2019. Wind speed measurements and predictions over Belmont hill, Wellington, New Zealand. *Journal of Wind Engineering and Industrial Aerodynamics*, 195:104018. https://doi.org/10.1016/j.jweia.2019.104018

Han Y, Shen L, Xu GJ, et al., 2018. Multiscale simulation of wind field on a long-span bridge site in mountainous area. *Journal of Wind Engineering and Industrial Aerodynamics*, 177:260-274. https://doi.org/10.1016/j.jweia.2018.04.012

Hu P, Han Y, Xu GJ, et al., 2018. Numerical simulation of wind fields at the bridge site in mountain-gorge terrain considering an updated curved boundary transition section. *Journal of Aerospace Engineering*, 31(3):04018008. https://doi.org/10.1061/(ASCE)AS.1943-5525.0000830

Hu WC, Yang QS, Chen HP, et al., 2021. Wind field characteristics over hilly and complex terrain in turbulent boundary layers. *Energy*, 224:120070. https://doi.org/10.1016/j.energy.2021.120070

Ishihara T, Hibi K, Oikawa S, 1999. A wind tunnel study of turbulent flow over a three-dimensional steep hill. *Journal of Wind Engineering and Industrial Aerodynamics*, 83(1-3):95-107. https://doi.org/10.1016/S0167-6105(99)00064-1

Ishihara T, Qian GW, Qi YH, 2020. Numerical study of turbulent flow fields in urban areas using modified k–ε model and large eddy simulation. *Journal of Wind Engineering and Industrial Aerodynamics*, 206:104333. https://doi.org/10.1016/j.jweia.2020.104333

Jiang FY, Zhang MJ, Li YL, et al., 2021. Field measurement study of wind characteristics in mountain terrain: focusing on sudden intense winds. *Journal of Wind Engineering and Industrial Aerodynamics*, 218:104781. https://doi.org/10.1016/j.jweia.2021.104781

Jing HM, Liao HL, Ma CM, et al., 2019. Influence of elevated water levels on wind field characteristics at a bridge site. *Advances in Structural Engineering*, 22(7):1783-1795. https://doi.org/10.1177/1369433218825048

Liu ZQ, Ishihara T, He XH, et al., 2016. LES study on the turbulent flow fields over complex terrain covered by vegetation canopy. *Journal of Wind Engineering and Industrial Aerodynamics*, 155:60-73. https://doi.org/10.1016/j.jweia.2016.05.002

Lund TS, Wu XH, Squires KD, 1998. Generation of turbulent inflow data for spatially-developing boundary layer simulations. *Journal of Computational Physics*, 140(2):233-258. https://doi.org/10.1006/jcph.1998.5882

Ma YL, Liu HP, 2017. Large-eddy simulations of atmospheric flows over complex terrain using the immersed-boundary method in the weather research and forecasting model.

Boundary-Layer Meteorology, 165(3):421-445.
https://doi.org/10.1007/s10546-017-0283-9

MOT (Ministry of Transport of the People's Republic of China), 2018. Wind-Resistant Design Specification for Highway Bridges, JTG/T 3360-01-2018. National Standards of the People's Republic of China (in Chinese).

NRCC (National Research Council of Canada), 2020. National Building Code User's Guide–Structural Commentaries (Part 4), NRCC2020. Canadian Commission on Building and Fire Codes, NRCC, Ottawa, Canada.

Pirooz AAS, Flay RGJ, Turner R, 2021. New Zealand design wind speeds, directional and lee-zone multipliers proposed for AS/NZS 1170.2:2021. *Journal of Wind Engineering and Industrial Aerodynamics*, 208:104412.
https://doi.org/10.1016/j.jweia.2020.104412

Ren HH, Laima SJ, Chen WL, et al., 2018. Numerical simulation and prediction of spatial wind field under complex terrain. *Journal of Wind Engineering and Industrial Aerodynamics*, 180:49-65.
https://doi.org/10.1016/j.jweia.2018.07.012

Tang HJ, Li YL, Shum KM, et al., 2020. Non-uniform wind characteristics in mountainous areas and effects on flutter performance of a long-span suspension bridge. *Journal of Wind Engineering and Industrial Aerodynamics*, 201:104177.
https://doi.org/10.1016/j.jweia.2020.104177

Tang XY, Zhao SM, Fan B, et al., 2019. Micro-scale wind resource assessment in complex terrain based on CFD coupled measurement from multiple masts. *Applied Energy*, 238:806-815.
https://doi.org/10.1016/j.apenergy.2019.01.129

Uchida T, Ohya Y, 2003. Large-eddy simulation of turbulent airflow over complex terrain. *Journal of Wind Engineering and Industrial Aerodynamics*, 91(1-2):219-229.
https://doi.org/10.1016/S0167-6105(02)00347-1

Wang T, Cao SY, Ge YJ, 2014. Effects of inflow turbulence and slope on turbulent boundary layer over two-dimensional hills. *Wind and Structures*, 19(2):219-232.
https://doi.org/10.12989/was.2014.19.2.219

Xing LF, Zhang MJ, Li YL, et al., 2021. Large eddy simulation of the fluctuating wind environment at a bridge site in the mountainous area. *Advances in Bridge Engineering*, 2(1):26.
https://doi.org/10.1186/s43251-021-00049-4

Yan L, Guo ZS, Zhu LD, et al., 2016. Wind tunnel study of wind structure at a mountainous bridge location. *Wind and Structures*, 23(3):191-209.
https://doi.org/10.12989/was.2016.23.3.191

Yang QS, Zhou T, Yan BW, et al., 2020. LES study of turbulent flow fields over hilly terrains—comparisons of inflow turbulence generation methods and SGS models. *Journal of Wind Engineering and Industrial Aerodynamics*, 204:104230.
https://doi.org/10.1016/j.jweia.2020.104230

Yang QS, Zhou T, Yan BW, et al., 2021. LES study of topographical effects of simplified 3D hills with different slopes on ABL flows considering terrain exposure conditions. *Journal of Wind Engineering and Industrial Aerodynamics*, 210:104513.
https://doi.org/10.1016/j.jweia.2020.104513

Zhang MJ, Li YL, Wang B, et al., 2018. Numerical simulation of wind characteristics at bridge site considering thermal effects. *Advances in Structural Engineering*, 21(9):1313-1326.
https://doi.org/10.1177/1369433217742524

Zhang MJ, Jiang FY, Li YL, et al., 2022. Multi-point field measurement study of wind characteristics in mountain terrain: focusing on periodic thermally-developed winds. *Journal of Wind Engineering and Industrial Aerodynamics*, 228:105102.
https://doi.org/10.1016/j.jweia.2022.105102

Zhou T, Yang QS, Yan BW, et al., 2022a. Detached eddy simulation of turbulent flow fields over steep hilly terrain. *Journal of Wind Engineering and Industrial Aerodynamics*, 221:104906.
https://doi.org/10.1016/j.jweia.2022.104906

Zhou T, Yan BW, Yang QS, et al., 2022b. POD analysis of spatiotemporal characteristics of wake turbulence over hilly terrain and their relationship to hill slope, hill shape and inflow turbulence. *Journal of Wind Engineering and Industrial Aerodynamics*, 224:104986.
https://doi.org/10.1016/j.jweia.2022.104986